

Journal of Materials Chemistry A

Accepted Manuscript



This is an *Accepted Manuscript*, which has been through the Royal Society of Chemistry peer review process and has been accepted for publication.

Accepted Manuscripts are published online shortly after acceptance, before technical editing, formatting and proof reading. Using this free service, authors can make their results available to the community, in citable form, before we publish the edited article. We will replace this *Accepted Manuscript* with the edited and formatted *Advance Article* as soon as it is available.

You can find more information about *Accepted Manuscripts* in the [Information for Authors](#).

Please note that technical editing may introduce minor changes to the text and/or graphics, which may alter content. The journal's standard [Terms & Conditions](#) and the [Ethical guidelines](#) still apply. In no event shall the Royal Society of Chemistry be held responsible for any errors or omissions in this *Accepted Manuscript* or any consequences arising from the use of any information it contains.

Cite this: DOI: 10.1039/c0xx00000x

www.rsc.org/xxxxxx

Remarkable oxygen barrier films based on layered double hydroxide/chitosan hierarchical structure

Ting Pan, Simin Xu, Yibo Dou, Xiaoxi Liu, Zhongze Li, Jingbin Han,* Hong Yan and Min Wei

Received (in XXX, XXX) Xth XXXXXXXXXX 20XX, Accepted Xth XXXXXXXXXX 20XX

DOI: 10.1039/b000000x

Abstract: High performance gas barrier film was fabricated *via* alternate spin-coating of chitosan (CTS) and hierarchical layered double hydroxide (H-LDH). The H-LDH synthesized by calcination-rehydration method shows hierarchical structure with nanowalls aligned vertically on the LDH platelets, which was subsequently assembled in CTS matrix, generating a hybrid film with excellent gas barrier property. Compared with the (P-LDH/CTS)₁₀ barrier film based on plate-like LDH (P-LDH), the (H-LDH/CTS)₁₀ film exhibits significantly enhanced oxygen barrier property with an oxygen transmission rate (OTR) below the detection limit of commercial instrument (<0.005 cm³ m⁻² day⁻¹ atm⁻¹). The greatly improved performance of (H-LDH/CTS)₁₀ film is attributed to the tortuous diffusion path in hierarchical architecture space. Moreover, experimental results and theoretical calculations reveal the existence of the adhesive force between oxygen and H-LDH (adsorption energy=-2.46 eV), which further reduces the oxygen diffusion rate and thus promotes oxygen barrier property. Therefore, this work provides a facile and cost-effective strategy to fabricate high gas barrier material, which can serve as a promising candidate for food/pharmaceutical packaging and encapsulation of electronic devices.

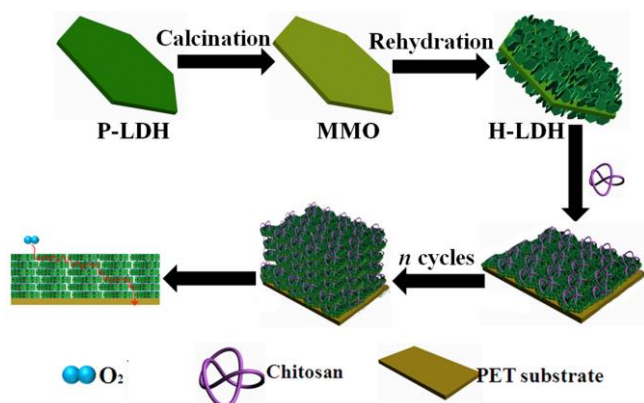
1. Introduction

Polymer films have been applied as packaging materials due to their light-weight, low-cost and good processability. However, their application as gas barrier materials is restricted because of a relatively high gas permeability.¹⁻³ In order to meet the extremely requirements for gas barrier in food packaging, membrane separation and encapsulation of flexible electronic devices,⁴⁻⁶ a wide variety of hybrid materials containing polymer and two-dimensional (2D) inorganic platelets have been designed and fabricated.⁷⁻¹⁰ For instance, clay and graphene were incorporated into polymer matrix to achieve high-performance gas barrier materials with low oxygen transmission rate and high transparency.^{11,12} Since the infilling of high-oriented platelets into polymer matrix would induce a long diffusion length and strong resistance to permeating gas, considerable efforts have been devoted to the synthesis of organic-inorganic composites as gas barrier materials. Nevertheless, for such a brick-and-mortar structure, the diffusion of gas molecules is only suppressed in the normal direction of the films,^{13,14} i.e., the gas diffusion parallel to the inorganic platelets is non-restricted. As a consequence, the mass loading of inorganic platelets would be very high to meet the requirement of low gas permeability, which finally results in poor flexibility and inferior toughness of the barrier materials. Furthermore, the aggregation of polymer is normally inevitable due to the disordered structure and intertwist of cross-linkers, leading to a tremendous free volume for gas molecule diffusion,

which is unfavorable to the suppression of gas permeability.¹⁵ These issues are serious problems in the enhancement of gas barrier property for practical applications. Therefore, how to develop superb barrier films that restrain gas migration effectively is still a challenging goal.

Layered double hydroxides (LDHs) are a kind of important 2D layered materials, whose structure can be generally expressed as [M^{II}_{1-x}M^{III}_x(OH)₂](Aⁿ⁻)_{x/n}mH₂O (M^{II} and M^{III} are divalent and trivalent metals, respectively, Aⁿ⁻ is the interlayer anion).¹⁶⁻¹⁹ Recently, various LDHs with hierarchical architecture have been widely investigated in gas adsorption and separation,²⁰ energy storage,²¹ catalysis²² and pharmaceutical fields²³ due to their large surface area and high exposure of active sites. Our previous work reported the plate-like LDH assembled with polymer matrix dramatically inhibits the diffusion of oxygen molecules across the hybrid film.²⁴ However, the gas barrier property was not satisfactory in the case of very thin films (for instance, <5 μm). If a LDH with hierarchical architecture is incorporated with polymer, the resulting hybrid films as barrier materials would possess the following advantages even with less thickness: firstly, hierarchical LDH is capable of restraining the migration of oxygen from multiple directions, inducing more tortuous pathway for oxygen diffusion; secondly, a large amount of oxygen molecules could be adsorbed on the surface of hierarchical LDH due to its high surface area, which may fill in the free volume between LDH and polymer and consequently produce low gas diffusion rate.

In this work, hierarchical LDH (H-LDH) was synthesized by a continuous calcination-rehydration treatment of plate-like LDH (P-LDH), which was then used as building block to fabricate multilayer films with chitosan (CTS) by alternate spin-coating technique (Scheme 1). The resulting (H-LDH/CTS)_n film exhibits ultrahigh gas barrier behavior with an oxygen transmission rate (OTR) below the detection limit of commercial instrument (<0.005 cm³ m⁻² day⁻¹ atm⁻¹). In addition, the (H-LDH/CTS)_n film displays excellent storage and thermal stabilities, which would guarantee its practical applications in food/pharmaceutical packing and electronic encapsulation.



Scheme 1. Schematic representation for the fabrication of (H-LDH/CTS)_n films with excellent oxygen barrier property.

2. Experimental Section

2.1 Materials

Chitosan (CTS) was purchased from Sigma-Aldrich Co. Ltd. Analytical grade chemicals including Mg(NO₃)₂·6H₂O, Al(NO₃)₃·9H₂O, urea, ethanol and acetone were used without further purification. Deionized water was used in all the experimental processes.

2.2 Synthesis of plate-like LDH

Plate-like LDH (P-LDH) was prepared by a hydrothermal method, which was reported in our previous work.²⁵ Typically, 1 mmol Mg(NO₃)₂·6H₂O, 0.5 mmol Al(NO₃)₃·9H₂O, 5 mmol urea were dissolved in 100 ml of water and transferred into a Teflon lined stainless steel autoclave. Subsequently, the autoclave was sealed and hydrothermally treated at 110 °C for 24 h. The powdered P-LDH sample was obtained *via* centrifugation, washing thoroughly and drying at 60 °C for 12 h.

2.3 Synthesis of hierarchical LDH

The obtained P-LDH powdered sample was calcined in a muffle furnace at 450 °C for 3 h, with a heating rate of 2 °C/min. After calcination, LDH phase was transformed into mixed metal oxides (MMO) with a porous structure. The MMO sample (0.2 g) was then placed into 1 M NaOH solution followed by stirring vigorously for 120 min at room temperature. Then hierarchical LDH (H-LDH) paste was obtained after washing twice with deionized water, followed by centrifugation. Subsequently, the H-LDH paste was dispersed in 400 ml of deionized water for the fabrication of (H-LDH/CTS)_n films.

2.4 Fabrication of (H-LDH/CTS)_n hybrid films

The (H-LDH/CTS)_n multilayer films were constructed by applying the spin-coating technique. Prior to deposition, the poly(ethylene terephthalate) (PET) substrates were treated in an ultrasonic bath with deionized water, ethanol, acetone for 10 min, respectively. Chitosan (3 g) was dissolved in deionized water (100 ml) containing 2 wt.% acetic acid. After vigorously stirred for 24 h, it was expected that the amine groups of chitosan were fully protonated by the acetic acid.

The H-LDH suspension and CTS solution were spin-coated onto a pre-cleaned PET substrate with 2500 rpm for 60 s and 4500 rpm for 60 s alternately. The film was dried at ambient temperature in air for 20 min after each spin-coating process. Subsequently, a series of these operations for H-LDH and CTS were repeated *n* times to obtain the (H-LDH/CTS)_n multilayer films. As comparison samples, the (P-LDH/CTS)_n and pure CTS films were fabricated by a similar spin-coating process.

2.5 Characterization techniques

X-ray diffraction (XRD) patterns were recorded by a Rigaku XRD-6000 diffractometer, using Cu Kα radiation (λ = 0.1542 nm) at 40 kV, 30 mA. Fourier transform infrared (FT-IR) spectra were obtained using a Vector 22 (Bruker) spectrophotometer with 2 cm⁻¹ resolution. UV-vis absorption spectra were collected in the range 200–800 nm on a Shimadzu U-3000 spectrophotometer. X-ray photoelectron spectra (XPS) were recorded on a Thermo VG Escalab 250 X-ray photoelectron spectrometer at a pressure of about 2 × 10⁻⁹ Pa with Al Kα X-rays as the excitation source. The morphology was investigated using a scanning electron microscope (SEM; Zeiss SUPRA 55) with the accelerating voltage of 20 kV, a FEI Cs-corrected Titan 80-300 high resolution transmission electron microscope (HRTEM) operated at 300 kV and a NanoScope IIIa atomic force microscope (AFM) from Veeco Instruments. The specific surface area was performed by Brunauer-Emmett-Teller (BET) method by use of a Quantachrome Autosorb-IC-VP analyzer. Thermogravimetry (TG) curve was obtained on a Beifen PCT-IA instrument in the temperature range 30–650 °C. Temperature programmed desorption (TPD) measurements were carried out on a Micromeritics AutoChem II 2920 automated characterization system. Positron annihilation measurements were taken with a fast-slow coincidence ORTEC system with a time resolution of 187 ps for the full width at half-maximum. Oxygen transmission rates (OTRs) were collected using VAC-V2 gas transmission rate testing equipment. All permeability coefficient values were averaged from at least five separate films.

3. Result and discussion

3.1 Preparation and characterization of H-LDH

The H-LDH sample with a hierarchical structure was synthesized by the following three-step route: hydrothermal synthesis of P-LDH, calcination of P-LDH to MMO and subsequent rehydration treatment. The pristine P-LDH, calcined sample and reconstructed H-LDH were firstly characterized by powder X-ray diffraction (XRD) measurements (Fig. 1). For pristine P-LDH sample (curve a), the peaks at 2θ = 12.18°, 24.31°, 35.96°, 39.15°, 47.22°, 61.22° and 62.31° are attributed to the (003), (006), (009),

(015), (018), (110) and (113) facet of LDH phase. The characteristic reflections (200) and (220) ascribed to crystalline MgO phase were detected after calcination (curve b), indicating the occurrence of phase transition from LDH to MMO. After rehydration, the reappearance of original LDH peaks (curve c) indicates the back-transformation from MMO to LDH phase, owing to the well-recognized memory effect.²⁶ Moreover, the XRD patterns of the samples with various rehydration times are shown in Fig. S1 (see ESI†). The intensity increases gradually upon prolonging the rehydration time from 1 h to 6 h, indicating the gradual growth of reconstructed H-LDH.

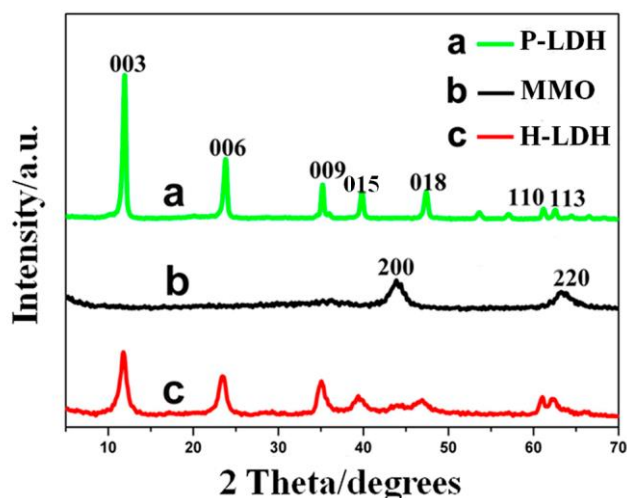


Fig. 1 XRD patterns of the (a) as-prepared P-LDH, (b) MMO, and (c) reconstructed H-LDH sample, respectively.

The structure and morphology details of as-prepared LDH, MMO and reconstructed H-LDH samples were investigated by SEM and TEM. Top-view SEM image of the pristine LDH shows hexagonal plate-like microcrystals with diameter of 2.0–2.5 μm (Fig. 2A). Calcination of the P-LDH leads to its transformation to MMO, whose SEM image shows that MMO inherits the original hexagonal morphology of the P-LDH precursor (Fig. 2B). It is worth noting that a large number of small nanowalls vertically aligned on the original large plate of LDH were observed after reconstruction (Fig. 2C), giving rise to hierarchical architecture. Meanwhile, the corresponding energy dispersive X-ray spectroscopy (EDX) mapping reveals the magnesium, aluminium and oxygen element are homogeneously distributed throughout the H-LDH (Fig. 2D). Moreover, the TEM images of P-LDH, MMO and H-LDH (Fig. 3A, 3B and 3C) further illustrate the phase transition process, in accordance with the XRD and SEM results. In addition, HR-TEM image shows the lattice fringe of 0.26 nm (Fig. 3D), which is attributed to the (012) plane of the LDH phase.

The N_2 adsorption-desorption measurements were carried out to study the surface area of original P-LDH and reconstructed H-LDH sample (Fig. 4A). Both the samples exhibit typical IV isotherm with a H3-type hysteresis loop ($P/P_0 > 0.4$), indicating the presence of mesopores. The H-LDH exhibits much larger specific surface area ($154.3 \text{ m}^2 \text{ g}^{-1}$) than that of P-LDH sample ($57.8 \text{ m}^2 \text{ g}^{-1}$), due to the existence of abundant nanowalls on the surface of microcrystal. Since the interaction between the barrier film and permeating gas is a crucial key for barrier property, O_2

temperature programmed desorption (TPD) was performed to detect the binding capacity for P-LDH and H-LDH to O_2 molecule. As shown in Fig. 4B, the O_2 TPD profile of the H-LDH sample (curve b) displays a desorption peak located at $164 \text{ }^\circ\text{C}$. In contrast to that of H-LDH, no apparent peak is observed for the P-LDH sample (curve a). This result illustrates the existence of

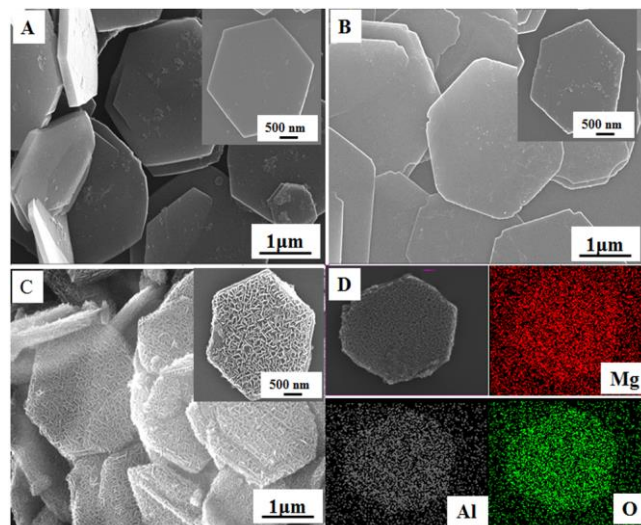


Fig. 2 SEM images of the (A) P-LDH (inset: a single P-LDH microcrystal), (B) MMO (inset: a single MMO microcrystal) and (C) H-LDH (inset: a single H-LDH microcrystal), respectively. (D) EDX mapping results for a single microcrystal of H-LDH.

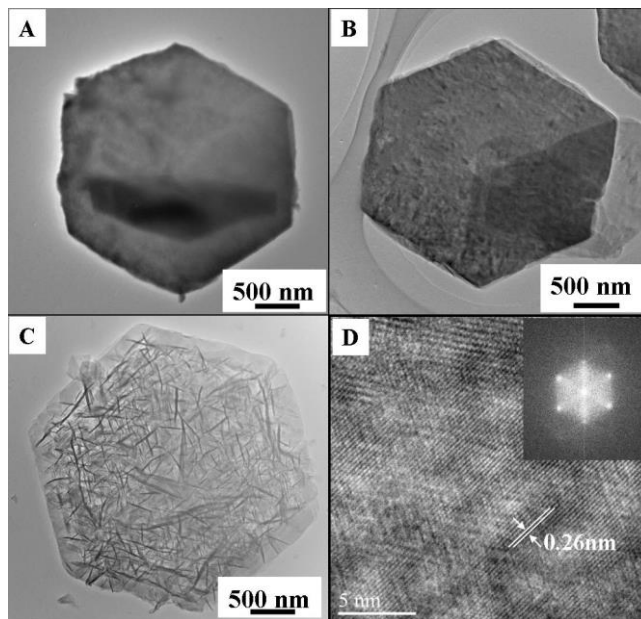


Fig. 3 TEM images of the (A) P-LDH, (B) MMO and (C) H-LDH. (D) The lattice fringe of H-LDH (inset: the fast Fourier transform pattern).

strong chemisorption between H-LDH and oxygen molecule due to the emerging of oxygen vacancies accompanied by the reconstruction of LDH. The oxygen vacancies serving as capture traps would adsorb the permeating oxygen and consequently inhibit the gas diffusion. Therefore, the H-LDH could be an ideal building block for the fabrication of oxygen barrier films.

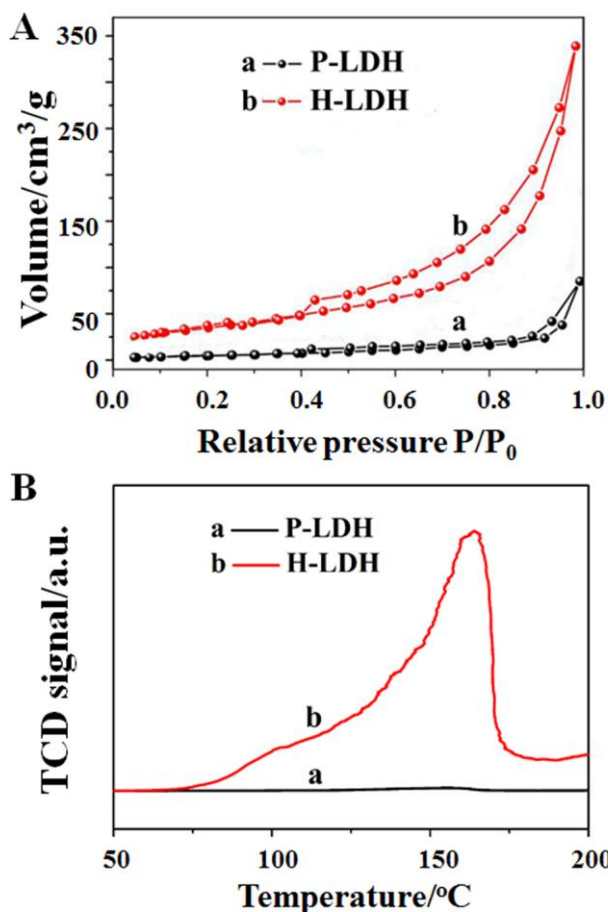


Fig. 4 (A) The N₂ adsorption-desorption isotherms and (B) O₂ TPD profiles for (a) P-LDH and (b) H-LDH sample, respectively.

3.2 Fabrication, structural and morphological study of (H-LDH/CTS)_n films

The H-LDH sample was used as building blocks to fabricate (H-LDH/CTS)_n films by the alternate spin-coating technique. UV-vis absorption spectra of the (H-LDH/CTS)_n films with various bilayer numbers are shown in Fig. 5. The characteristic absorption intensity of CTS at 200 nm enhances linearly with the increase of bilayer number *n* (Fig. 5, inset), indicating a stepwise and regular growth process for the (H-LDH/CTS)_n films. X-ray photoelectron spectroscopy (XPS) spectra were investigated to illustrate the interactions between H-LDH and CTS (Fig. S2, ESI†). For pure H-LDH and CTS polymer, the binding energies of Mg 1s, Al 2p and C 1s are located at 1304.4, 74.1 and 285.7 eV, respectively. After the combination of H-LDH with CTS, the binding energies of Mg 1s and Al 2p increase to 1305.2 and 74.8 eV. Concomitantly, a decreased binding energy of C 1s (C–O–H in CTS) from 285.7 to 284.4 eV is observed. The binding energy shift is indicative of an increased oxidation state of Mg and Al in H-LDH while a decreased binding energy of C in CTS polymer, possibly owing to the formation of hydrogen bonding between H-LDH and CTS.

XRD pattern (Fig. S3, ESI†) of the obtained (H-LDH/CTS)₁₀ film displays a peak at $2\theta = 12.18^\circ$, which is attributed to the (003) reflection of the H-LDH structure. Moreover, this film

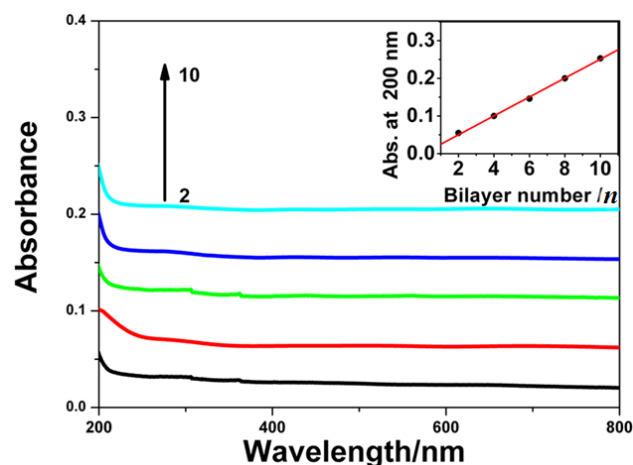


Fig. 5 UV-vis absorption spectra of the (H-LDH/CTS)_n (*n* = 2–10) films on quartz glass substrates (inset: the linear relationship between absorbance at 200 nm and bilayer number *n*).

exhibits remarkable transparency with an average light transmittance of 80% across the visible-light spectrum (400–800 nm, Fig. S4, ESI†). The AFM topographical image shown in Fig. 6A gives the morphology and roughness information of the (H-LDH/CTS)₁₀ film, from which a root-mean square roughness of ~15.9 nm is observed. Additionally, the surface roughness of the as-prepared (H-LDH/CTS)_n films (Fig. S5, ESI†) increases to ~6.3, ~10.6 and ~15.9 nm upon increasing the assembled bilayer to 3, 6 and 10. The typical top-view SEM image of (H-LDH/CTS)₁₀ film (Fig. 6B) shows the small platelets are aligned vertically in the CTS matrix; a film thickness of ~360 nm is observed from its side-view SEM image (Fig. 6B, inset). Elements line scanning profile (Fig. 6C) along the cross section further verifies the homogeneous distribution of magnesium, aluminium, oxygen and carbon throughout the (H-LDH/CTS)₁₀ film. Furthermore, no delamination or peeling occurred upon scratching of the film surface, indicating a strong adhesion of the film to the substrate (Fig. S6, ESI†).

It is well known that the free volume of barrier material is closely related to their gas permeability.²⁷ Thus, positron annihilation lifetime spectroscopy (PALS) was applied as a quantitative probe to explore the fraction of free volume (*F_v*). Fig. 6D shows the *F_v* values for pristine PET, (P-LDH/CTS)₁₀ and (H-LDH/CTS)₁₀ film, respectively, which are obtained based on positron lifetime component (τ_3) as well as relative intensity (*I₃*) (Fig. S7A and S7B, see details in ESI†). For pristine PET substrate, the free volume is 14.41%. After combination with P-LDH, the *F_v* decreases to 10.64%, illustrating the incorporated LDH platelets reduces the free volume fraction. Moreover, further reduction of *F_v* (8.88%) is observed for (H-LDH/CTS)₁₀ film, which is attributed to the suppression of polymer mobility by vertically aligned nanowalls in the H-LDH. The decreased *F_v* value together with strong chemisorption between H-LDH and oxygen molecule (from TPD result, Fig. 4B) plays an important role in promotion of gas barrier property, which will be discussed in the next section.

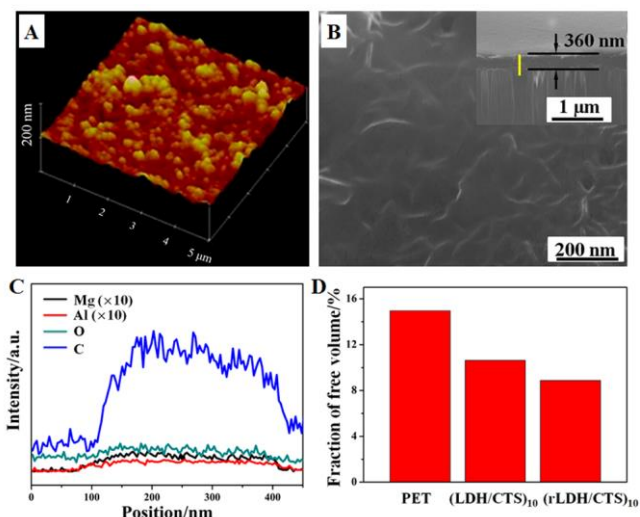


Fig. 6 (A) AFM image, (B) top-view SEM image (inset: side-view SEM image), (C) elements line scanning along the cross section of (H-LDH/CTS)₁₀ film, (D) free volume fraction of the pristine PET substrate, (P-LDH/CTS)₁₀ and (H-LDH/CTS)₁₀ film, respectively.

3.3 The investigation of oxygen barrier property for the (H-LDH/CTS)_n films

The oxygen transmission rate (OTR) was measured to investigate the barrier property of (P-LDH/CTS)_n and (H-LDH/CTS)_n films (Fig. 7). The pristine PET substrate displays an OTR of ~ 8.431 $\text{cm}^3 \text{m}^{-2} \text{day}^{-1} \text{atm}^{-1}$. The coating of (P-LDH/CTS)_n and (H-LDH/CTS)_n films leads to a dramatically decrease in OTR. Fig. 7 shows the OTR values for (P-LDH/CTS)_n films decrease from ~ 6.71 to ~ 0.5 $\text{cm}^3 \text{m}^{-2} \text{day}^{-1} \text{atm}^{-1}$ with increasing bilayer number n from 3 to 10. In contrast to (P-LDH/CTS)₁₀ film, pure CTS film with the same thickness displays relatively weak barrier ability with OTR of ~ 3.824 $\text{cm}^3 \text{m}^{-2} \text{day}^{-1} \text{atm}^{-1}$ (Fig. S8, ESI†). This results illustrate the incorporation of highly-oriented P-LDH platelets suppresses the diffusion of oxygen, as a result of the increased oxygen diffusion length in vertical direction. In addition, the (H-LDH/CTS)_n films display a superior oxygen barrier property to (P-LDH/CTS)_n films. The OTR of (H-LDH/CTS)₁₀ film decreases dramatically with a value below the detection limit of commercial instrumentation (< 0.005 $\text{cm}^3 \text{m}^{-2} \text{day}^{-1} \text{atm}^{-1}$). The improved oxygen barrier property is mainly attributed to the following two factors: firstly, H-LDH is capable of restraining the migration of oxygen both in vertical and parallel direction (Fig. S9, ESI†) owing to its unique hierarchical structure; secondly, the oxygen vacancies on H-LDH surface serve as capture traps to absorb permeating oxygen, which results in a decreased free volume and further enhancement of the barrier property.

Taking into account potential applications of oxygen barrier films, the stability of (H-LDH/CTS)₁₀ film was further studied. The storage stability test was carried out after six months of storage (Fig. S10, ESI†). No obvious change in OTR value is observed, which illustrates the (H-LDH/CTS)₁₀ film possesses excellent storage stability. Moreover, the weight of (H-LDH/CTS)₁₀ film does not show obvious loss until the temperature increases to ~ 200 °C (Fig. S11, ESI†), indicating the high thermal stability of (H-LDH/CTS)₁₀ film. Therefore, the ultrahigh oxygen barrier property, together with the satisfactory

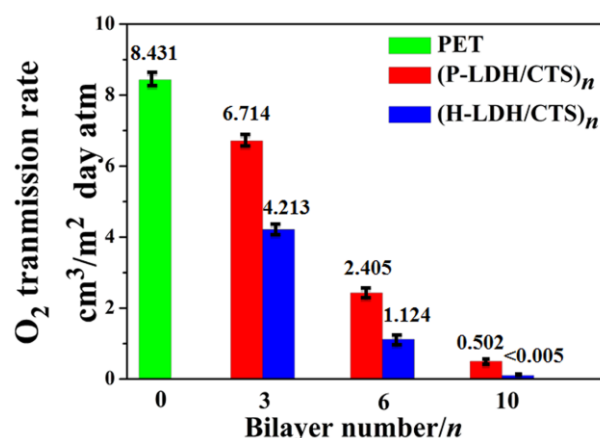


Fig. 7 Oxygen transmission rate values for pristine PET, (P-LDH/CTS)_n and (H-LDH/CTS)_n films on PET substrate ($n = 3, 6, 10$), respectively.

storage and thermal stabilities, would hold promise for its prospective applications.

3.4 Computational simulation

Molecular dynamics (MD) simulations were further carried out to give a deep insight into the thermal motion of oxygen in H-LDH/CTS films (see details in ESI†). After molecule dynamics simulation of 1000 ps, the geometry of H-LDH/CTS system is displayed in Fig. 8A. The binding energy between H-LDH and CTS is calculated to be as high as -0.83 eV per CTS monomer based on first-principle. The strong interaction indicates the existence of hydrogen bonding network (blue dashed line in Fig. 8B) in this system, which was also confirmed by XPS results (Fig. S2, ESI†). Moreover, the interactions between oxygen and H-LDH surface were also investigated based on density functional theory calculation. The adsorption energy of oxygen on the surface of H-LDH is -2.46 eV, which is much larger than that on P-LDH (-0.03 eV), indicating the stronger chemical interaction between oxygen and H-LDH. The geometries of oxygen interacting with H-LDH/CTS and P-LDH/CTS (as control sample) systems are shown in Fig. 8C and 8D, respectively. The results show that the oxygen molecule is adsorbed on the H-LDH surface at the oxygen vacancy (Fig. 8C); while the oxygen molecule is located on the surface of P-LDH flatly (Fig. 8D). Therefore, the result illustrates that the oxygen is trapped on the surface of H-LDH by oxygen vacancies, which depresses the oxygen diffusion rate.

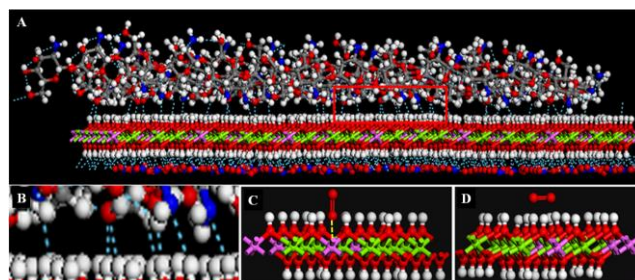


Fig. 8 (A) The geometry of H-LDH/CTS system after molecular dynamics simulation of 1000 ps; (B) the amplified picture of the red zone in (A), the blue dashed line in (A) and (B) represents the hydrogen bond; the optimized geometries of oxygen adsorbing on (C) H-LDH and (D) P-LDH.

4. Conclusions

In summary, we demonstrate the fabrication of (H-LDH/CTS)_n multilayer films with remarkable gas barrier property through cost-effective spin-coating technique. The H-LDH with hierarchical architecture plays a key role in improvement of oxygen barrier property: (1) the H-LDH could inhibit the diffusion of oxygen molecule in both vertical and parallel directions, which introduces longer pathway for oxygen permeation in comparison with P-LDH; (2) the oxygen diffusion rate is depressed by strong interfacial chemisorption between oxygen and (H-LDH/CTS)_n films, due to the presence of oxygen vacancies on H-LDH surface. In addition, the (H-LDH/CTS)_n film represents high stability as well as long-term maintenance. Therefore, this work offers a promising strategy for the development of novel gas barrier materials, which are needed for a variety of applications, including food/pharmaceutical packaging, electronics encapsulation and related areas.

Acknowledgements

This work was supported by the 863 Program (Grant No. 2013AA032501), the National Natural Science Foundation of China (NSFC), the Doctoral Fund of Ministry of Education of China (20120010120010), and the Fundamental Research Funds for the Central Universities (YS1406). M. Wei particularly appreciates the financial aid from the China National Funds for Distinguished Young Scientists of the NSFC. We acknowledge National Supercomputing Center in Shenzhen for providing the computational resources and materials studio (version 6.1, CASTEP module).

Notes and references

State Key Laboratory of Chemical Resource Engineering, Beijing University of Chemical Technology, Beijing, 100029, China. E-mail: hanjb@mail.buct.edu.cn. Fax: +86-10-64425385; Tel: +86-10-64412131

† Electronic Supplementary Information (ESI) available: [powder XRD patterns of reconstructed H-LDH powders (Fig. S1); XPS spectra for H-LDH, CTS and (H-LDH/CTS)₁₀ films (Fig. S2); XRD pattern of (H-LDH/CTS)₁₀ film (Fig. S3); UV-vis transmittance spectrum of (H-LDH/CTS)₁₀ film (Fig. S4); AFM images of (H-LDH/CTS)_n films (Fig. S5); SEM image of the (H-LDH/CTS)₁₀ film after scratching on its surface (Fig. S6); o-ps lifetime and intensity of PET, (P-LDH/CTS)₁₀ and (H-LDH/CTS)₁₀ films (Fig. S7); OTR values for PET, CTS and (H-LDH/CTS)₁₀ films (Fig. S8); schematic representation showing the possible oxygen barrier mechanism (Fig. S9); OTR values for (H-LDH/CTS)₁₀ film (Fig. S10); thermogravimetric curve for (H-LDH/CTS)₁₀ film (Fig. S11)]. See DOI: 10.1039/b000000x/

- H. Yao, H. Fang, Z. Tan, L. Wu and S. Yu, *Angew. Chem. Int. Ed.*, 2010, **122**, 2186.
- H. Bai, C. Huang, H. Xiu, Q. Zhang, H. Deng, K. Wang, F. Chen and Q. Fu, *Biomacromolecules*, 2014, **15**, 1507.
- Y. Yang, L. Bolling, M. Haile and J. C. Grunlan, *RSC Adv.*, 2012, **2**, 12355.
- (a) Y. Yang, L. Bolling, M. Haile and J. C. Grunlan, *RSC Adv.*, 2012, **2**, 12355; (b) J. C. Grunlan, A. Grigorian, C. B. Hamilton and A. R. Mehrabi, *J. Appl. Polym. Sci.*, 2004, **93**, 1102.
- (a) F. E. Eichie, R. S. Okor and R. Groning, *J. Appl. Polym. Sci.*, 2006, **99**, 725; (b) M. A. Priolo, K. M. Holder, S. M. Greenlee and J. C. Grunlan, *ACS Appl. Mater. Interfaces*, 2012, **4**, 5529.

- (a) R. S. Jagadish, B. Raj and M. R. Asha, *J. Appl. Polym. Sci.*, 2009, **113**, 3732; (b) C. Wu, T. Saito, S. Fujisawa, H. Fukuzumi and A. Isogai, *Biomacromolecules*, 2012, **13**, 1927.
- (a) M. A. Osman, V. Mittal, M. Morbidelli and U. W. Suter, *Macromolecules*, 2004, **37**, 7250.
- (a) R. K. Layek, A. K. Das, M. U. Park, N. H. Kim and J. H. Lee, *J. Mater. Chem. A*, 2014, **2**, 12158; (b) H. Yao, Z. Tan, H. Fang and S. Yu, *Angew. Chem. Int. Ed.*, 2010, **122**, 10325.
- (a) Y. Dou, A. Zhou, T. Pan, J. Han, M. Wei, D. G. Evans and X. Duan, *Chem. Commun.*, 2014, **50**, 7136; (b) K. S. Triantafyllidis, P. C. LeBaron, I. Park and T. J. Pinnavaia, *Chem. Mater.*, 2006, **18**, 4393.
- (a) A. J. Svagan, A. Åkesson, M. Cárdenas, S. Bulut, J. C. Knudsen, J. Risbo and D. Plackett, *Biomacromolecules*, 2012, **13**, 397; (b) H. Liu, T. Kuila, N. H. Kim, B. C. Ku and J. H. Lee, *J. Mater. Chem. A*, 2013, **1**, 3739.
- (a) M. A. Priolo, D. Gamboa, K. M. Holder and J. C. Grunlan, *Nano Lett.*, 2010, **10**, 4970; (b) M. A. Priolo, K. M. Holder, S. M. Greenlee, B. E. Stevens and J. C. Grunlan, *Chem. Mater.*, 2013, **25**, 1649.
- (a) Y. Yang, L. Bolling, M. A. Priolo and J. C. Grunlan, *Adv. Mater.*, 2013, **25**, 503; (b) C. Xiang, P. J. Cox, A. Kukovec, B. Genorio, D. P. Hashim, Z. Yan, Z. Peng, C. Hwang, G. Ruan, E. L. G. Samuel, P. M. Sudeep, Z. Konya, R. Vajtai, P. M. Ajayan and J. M. Tour, *ACS Nano*, 2013, **7**, 10380; (c) J. Lim, H. Yeo, M. Goh, B. Ku, S. G. Kim, H. S. Lee, B. Park and N. You, *Chem. Mater.*, 2015, **27**, 2040.
- (a) C. Wu, Q. Yang, M. Takeuchi, T. Saito and A. Isogai, *Nanoscale*, 2014, **6**, 392; (b) H. Huang, C. Liu, D. Li, Y. Chen, G. Zhong and Z. Li, *J. Mater. Chem. A*, 2014, **2**, 15853.
- J. T. Yoo, S. B. Lee, C. K. Lee, S. W. Hwang, C. R. Kim, T. Fujigaya, N. Nakashima and J. K. Shim, *Nanoscale*, 2014, **6**, 10824.
- M. W. Moller, T. Lunkenbein, H. Kalo, M. Schieder, D. A. Kunz and J. Brey, *Adv. Mater.*, 2010, **22**, 5245.
- (a) J. Han, Y. Dou, M. Wei, D. G. Evans and X. Duan, *Angew. Chem. Int. Ed.*, 2010, **49**, 2171; (b) Y. Gu, Z. Lu, Z. Chang, J. Liu, X. Lei, Y. Li and X. Sun, *J. Mater. Chem. A*, 2013, **1**, 10655; (c) Z. Xu and P. S. Braterman, *J. Mater. Chem.*, 2003, **13**, 268; (d) M. Merchan, T. S. Ouk, P. Kuba, K. Lang, C. Coelho, V. Verney, S. Commereuc, F. Leroux, V. Sol and C. Taviot-Guetho, *J. Mater. Chem. B*, 2013, **1**, 2139.
- (a) J. Y. Uan, J. K. Lin and Y. S. Tung, *J. Mater. Chem.*, 2010, **20**, 761; (b) L. Huang, J. Wang, Y. Gao, Y. Qiao, Q. Zheng, Z. Guo, Y. Zhao, D. O'Hare and Q. Wang, *J. Mater. Chem. A*, 2014, **2**, 18454; (c) F. Leroux and C. Taviot-Guetho, *J. Mater. Chem.*, 2005, **15**, 3628.
- (a) Z. Gu, H. Zuo, L. Li, A. Wu and Z. Xu, *J. Mater. Chem. B*, 2015, DOI: 10.1039/c5tb00248f; (b) G. R. Williams and D. O'Hare, *J. Mater. Chem.*, 2006, **16**, 3065; (c) K. L. Dagnon, S. Ambadapadi, A. Shaito, S. M. Ogbomo, V. DeLeon, T. D. Golden, M. Rahimi, K. Nguyen, P. S. Braterman and N. A. D'Souza, *J. Appl. Polym. Sci.*, 2009, **113**, 1905; (d) G. R. Williams, A. G. Dunbar, A. J. Beer, A. M. Fogg and D. O'Hare, *J. Mater. Chem.*, 2006, **16**, 1231.
- (a) D. Yan, J. Lu, M. Wei, S. Qin, L. Chen, S. Zhang, D. G. Evans and X. Duan, *Adv. Funct. Mater.*, 2011, **21**, 2497; (b) Z. Xu and P. S. Braterman, *Appl. Clay Sci.*, 2010, **48**, 235; (c) P. Vialat, F. Leroux, C. Taviot-Guetho, G. Villemure and C. Mousty, *Electrochim. Acta*, 2013, **107**, 599; (d) C. Markland, G. Williams and D. O'Hare, *J. Mater. Chem.*, 2011, **21**, 17896.
- (a) J. Wang, L. Huang, R. Yang, Z. Zhang, J. Wu, Y. Gao, Q. Wang, D. O'Hare and Z. Zhong, *Energy Environ. Sci.*, 2014, **7**, 3478; (b) Y. Huang and S. Cheng, *J. Mater. Chem. A*, 2014, **2**, 13452.
- (a) F. Ning, M. Shao, C. Zhang, S. Xu, M. Wei and X. Duan, *Nano Energy*, 2014, **7**, 134; (b) M. Shao, M. Wei and X. Duan, *Sci. China Chem*, 2015, **45**, 109; (c) M. Shao, F. Ning, Y. Zhao, J. Zhao, M. Wei, D. G. Evans and X. Duan, *Chem. Mater.*, 2012, **24**, 1192.
- (a) C. Li, Y. Dou, J. Liu, Y. Chen, S. He, M. Wei, D. G. Evans and X. Duan, *Chem. Commun.*, 2013, **49**, 9992; (b) M. Zhao, Q. Zhang, X. Jia, J. Huang, Y. Zhang and F. Wei, *Adv. Funct. Mater.*, 2010, **20**, 677; (c) Q. Zhang, M. Zhao, Y. Liu, A. Cao, W. Qian, Y. Lu and F. Wei, *Adv. Mater.*, 2009, **21**, 2876; (d) M. Zhao, Q. Zhang, J. Huang, J. Nie and F. Wei, *Carbon*, 2010, **48**, 3260.

- 23 (a) M. Shao, F. Ning, J. Zhao, M. Wei, D. G. Evans and X. Duan, *J. Am. Chem. Soc.*, 2012, **134**, 1071; (b) C. Chen, P. Wang, T. Lim, L. Liu, S. Liu and R. Xu, *J. Mater. Chem. A*, 2013, **1**, 3877; (c) Z. Gu, J. J. Athertonab and Z. Xu, *Chem. Commun.*, 2015, **51**, 3024.
- 5 24 Y. Dou, S. Xu, X. Liu, J. Han, H. Yan, M. Wei, D. G. Evans and X. Duan, *Adv. Funct. Mater.*, 2014, **24**, 514.
- 25 J. Han, J. Lu, M. Wei, Z. Wang and X. Duan, *Chem. Commun.*, 2008, **44**, 5188.
- 26 F. Wong and R. G. Buchheit, *Pro. Org. Coat*, 2004, **51**, 91.
- 10 27 A. Ammala, S. J. Pas, K. A. Lawrence, R. Stark, R. I. Webb and A. J. Hill, *J. Mater. Chem.*, 2008, **18**, 911.